Author/s:
Jain, SK;Syed, N;Balendhran, S;Abbas, SAT;Ako, RT;Low, MX;Lobo, C;Zavabeti, A;Murdoch, BJ;Gupta, G;Bhaskaran, M;Crozier, KB;Russo, SP;Daeneke, T;Walia, S

Title:
Atomically Thin Gallium Nitride for High-Performance Photodetection

Date:
2023

Citation:
Jain, S. K., Syed, N., Balendhran, S., Abbas, S. A. T., Ako, R. T., Low, M. X., Lobo, C., Zavabeti, A., Murdoch, B. J., Gupta, G., Bhaskaran, M., Crozier, K. B., Russo, S. P., Daeneke, T. & Walia, S. (2023). Atomically Thin Gallium Nitride for High-Performance Photodetection. Advanced Optical Materials, 11 (15), https://doi.org/10.1002/adom.202300438.

Atomically thin gallium nitride for high-performance photodetection

Shubhendra Kumar Jain,[1,2,3,4,*] Nitu Syed,[5,6] Sivacarendran Balendhran,[4] Sherif Abdulkader Tawfik Abbas,[7] Rajour Tanyi Ako,[1] Mei Xian Low,[1] Charlene Lobo,[8] Ali Zavabeti,[9] Billy J. Murdoch,[10] Govind Gupta,[2,3] Madhu Bhaskaran,[1,6] Kenneth B. Crozier,[6,11,12] Salvy P Russo,[4] Torben Daeneke,[3] Sumeet Walia[1,3,*]

[1] Functional Materials and Microsystems Research Group and the Micro Nano Research Facility, RMIT University, Melbourne, Victoria 3000, Australia

[2] Sensor Devices & Metrology Group, CSIR - National Physical Laboratory (CSIR-NPL), Dr K. S. Krishnan Road, New Delhi 110012, India

[3] Academy of Scientific & Innovative Research, (AcSIR), CSIR-HRDC Campus, Ghaziabad, Uttar Pradesh 201002, India

[4] School of Electrical Engineering and Computer Science, University of Ottawa, Advanced Research Complex, Ottawa, Ontario, K1N 6N5, Canada (Present Affiliation)

[5] School of Engineering, RMIT University, Melbourne, Victoria, 3000, Australia

[6] ARC Centre of Excellence for Transformative Meta-Optical Systems, The University of Melbourne, Parkville, VIC 3010, Australia

[7] ARC Centre of Excellence in Exciton Science, School of Science, RMIT University, Melbourne, VIC 3001, Australia

[8] School of Mathematical and Physical Sciences, University of Technology Sydney, Ultimo, NSW 2007, Australia

[9] Department of Chemical Engineering, The University of Melbourne, Parkville, VIC 3010, Australia

[10] RMIT Microscopy and Microanalysis Facility, RMIT University, Melbourne, VIC, 3001 Australia

This is the author manuscript accepted for publication and has undergone full peer review but has not been through the copyediting, typesetting, pagination and proofreading process, which may lead to differences between this version and the Version of Record. Please cite this article as doi: 10.1002/adom.202300438.

[11] School of Physics, The University of Melbourne, Parkville, VIC 3010, Australia

[12] Department of Electrical and Electronics Engineering, The University of Melbourne, Parkville, VIC 3010, Australia

[*] Corresponding authors email: shubhendra21@gmail.com; sumeet.walia@rmit.edu.au

Abstract

Gallium nitride (GaN) semiconductor technology has matured and commercialised over the last few decades, particularly for optoelectronic technologies in the UV-blue spectrum. In this timeframe, the emergence of atomically thin functional materials and the concurrent demands for miniaturisation has prompted research into unique features that appear due to quantum confinement effects. However, the lack of successful techniques to produce GaN with high aspect ratios, due to its non-layered crystal structure, has prevented access to these new properties in GaN that are predicted to appear at such scales. Here, we address this important gap by printing ultra-thin GaN nanosheets (~1.4 nm) with lateral dimensions on the millimetre scale using a simple two-step process that simultaneously allows the introduction of nitrogen point defects. This enabled demonstration of a broadband photoelectrical spectral response from UV (280 nm) to NIR (1080 nm). The GaN based photodetectors displayed excellent figures of merit, having a responsivity (2.72×10^4 A/W) up to four orders of magnitude higher than the commercial photodetectors at room temperature, despite being 10^2-10^3 times thinner. The photodetectors exhibited fast switching, with rise and decay time in the range of microseconds. Our state-of-the-art device performance originates from the ultra-thin nature of GaN nanosheets coupled with introduction of nitrogen point vacancies in the synthesis process. This work presents the opportunity to significantly expand the reach of GaN semiconductor technology and may lead to applications in high-performance miniaturised imaging systems, spectroscopy, communication and integrated optoelectronic circuits.

Keywords

Broadband photodetector, gallium nitride, liquid metal exfoliation, Two-dimensional materials

Introduction

Conventional III-nitride semiconductors such as GaN, AlN and InN have been a major focus in the last couple of decades.[1-6]. Owing to high carrier mobility, chemical and thermal stability, GaN has been widely explored for numerous applications in power electronics, radio frequency devices, analogue circuits, and optoelectronics.[6-8] GaN based power electronic devices have shown huge potential and are on the cusp of commercialization for applications including point of load converters, electric vehicles, and renewable energy.[2, 9-10] GaN based power mobile chargers are already in the market, and can charge batteries three times faster than conventional chargers. Optoelectronic devices such as photodetectors, light emitting diode, and solar cells are being studied to fulfil futuristic demands. Owing to wide bandgap energy, GaN based photodetectors respond to ultraviolet (UV) spectrum restricting its deployment for visible spectral detection. This limits it applicability for imaging, and communication applications.

Epitaxial GaN films are grown via plasma-assisted molecular beam epitaxy, plasma enhanced chemical vapour deposition, and metal organic chemical vapour deposition techniques, which are effective for thin films at micro-meter scale and nanostructured surfaces.[4, 11-13] The next step towards unravelling new properties entails concurrent miniaturisation and enhanced performance. This has already resulted in a rapid increase in investigations of nitrides and other materials in their atomically-thin forms akin to research in two-dimensional (2D) material systems.[14-17] The low scattering and large surface to volume ratio of atomically-thin materials make them potential candidates for electronics and optoelectronics applications.[18-20] Computational methods have predicted that the electronic properties of atomically thin GaN are superior to those of bulk GaN due to quantum confinement.[21-22] The lowest-exciton binding energy of monolayer and bilayer GaN are more than one order of magnitude higher than bulk GaN counterparts. Consequently, atomically thin GaN offers enhanced excitonic energy levels, which can improve the internal quantum efficiency of the devices. The atomically thin GaN also exhibits a blue shift in the bandgap energy due to the quantum confinement.

The stable wurtzite crystal structure of the bulk GaN restricts the achievement of atomically-thin GaN via the traditional exfoliation routes.[23] Redwing and Robinson *et al*. reported the

synthesis of 2D GaN at the graphene/SiC interface intercalated through the top graphene layer. However, this method yields GaN with lateral dimensions on only nanometre-scale.[24] Recently, low cost and large area synthesis of several material families have been realised via exfoliation from liquid metals, known as the liquid metal exfoliation (LME) method.[25-27] Therefore, it is an attractive proposition to synthesize GaN in its atomically thin form using the LME approach for deployment as functional layers for optoelectronic devices such as photodetectors.

This study uses a unique LME technique to produce ultra-thin GaN layers with lateral dimensions up to the millimetre-scale. The technique relies on a two-step process that starts with the squeeze-printing of ultra-thin Ga_2O_3, which is then converted into GaN using ammonolysis in a tube furnace (shown in **Figure 1(a)**). The synthesis process has already been reported in detail.[25] The use of the ammonolysis step also enables introduction of nitrogen point defects leading to additional energy states in the bandgap. Therefore, the synthesized large-area GaN nanosheets in this work can be deployed as ultrasensitive broadband photodetectors with more than four orders of magnitude higher responsivity (10^3–10^4 A/W) than commercial photodetectors and with detectivity in the range 10^9–10^{10} Jones for wavelengths ranging from 280 to 1080 nm. To the best of our knowledge, 2D GaN based UV-visible-NIR detectors have never been reported before. Considering the quest for miniaturisation, this work showcases a high-performance GaN photodetector with a ~1.4 nm thick functional layer. This provides an exciting pathway toward miniaturizing light detection devices, expanding their breadth of applications in integrated optoelectronic circuits, imaging, and communications.

Results

An optical image of the as-prepared GaN nanosheets on SiO_2 substrate (300-nm thick layer of SiO_2 on silicon as the substrate) is shown in **Figure 1**(b). It can be seen that millimetre-scale GaN nanosheets can be achieved. The AFM micrograph of the GaN nanosheets (highlighted with yellow broken lines) is displayed in **Figure 1**(c). The thickness profile of the GaN nanosheets was estimated across the green solid line shown in **Figure 1**(d). The thickness of GaN nanosheets is measured ~1.4 nm, which corresponds to three wurtzite GaN

monolayers.[25] The atomic structure of the synthesized GaN nanosheets was scrutinized via high resolution transmission electron microscopy (HRTEM). High-temperature resistant Si_3N_4 grids were utilised for imaging the LME synthesized GaN nanosheets.[28-29] TEM imaging reveals translucent sheets indicating ultrathin nature of the GaN nanosheets, as shown in **Figure 1**(e). **Figure 1**(f) and (g) display the atomic resolution images and associated fast Fourier transform of the crystal lattice of GaN. High crystallinity of the synthesized nanosheets is observed where a lattice spacing is found to be ~0.26 nm which corresponds to the (002) planes of wurtzite GaN crystal structure.[30-31] The synthesized GaN nanosheets are polycrystalline and offer [002] facet as a dominant plane of orientation. The process temperature is one of the critical parameter which can control the presence of the defects and crystalline quality. The choice of substrate can influence the electrical and optical properties of the synthesized GaN nanosheets, but is out of the scope of this study. Further, these GaN nanosheets are observed to be thermodynamically stable which has been discussed in detail in a previous report.[25]

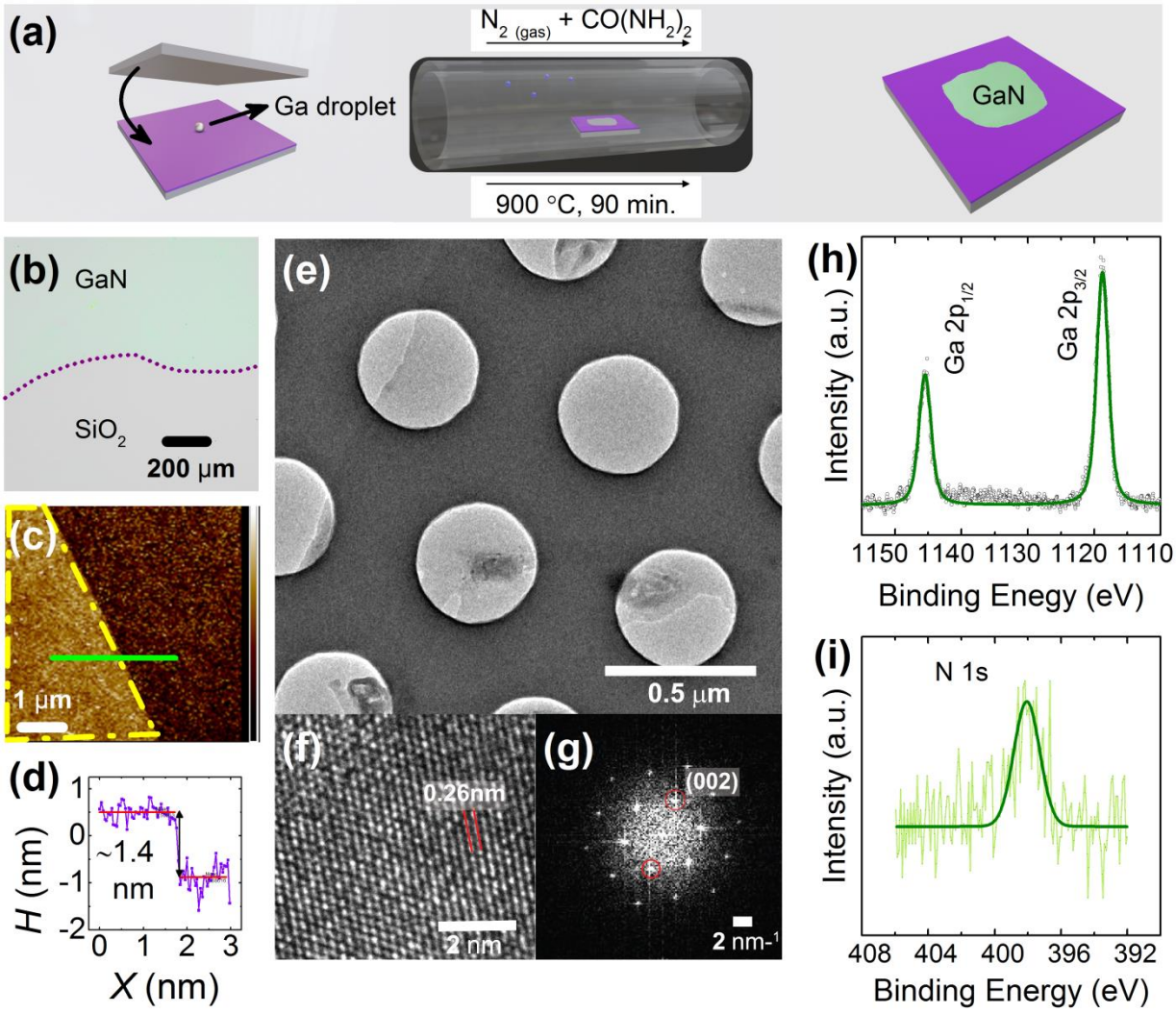

Figure 1. (a) Schematic representation of the liquid metal synthesis process of 2D GaN nanosheets. Squeeze-printing technique to deposit Ga_2O_3 on the substrate followed by the synthesis process of the 2D GaN nanosheets using ammonolysis of Ga_2O_3 and the synthesised 2D GaN nanosheets on the substrate. (b) An optical image of the synthesised large area 2D GaN on SiO_2 substrate via liquid metal exfoliation method. (c) AFM micrograph of the 2D GaN nanosheets with (d) height profile along with the green line. (e) HRTEM micrograph of the GaN film, (f) lattice fringes of the 2D GaN, and (g) FFT pattern demonstrating (002) plane of the GaN sheet. Fitted XPS spectra of the 2D GaN for (h) Ga 2p core level and (i) N 1s core level collected with Ag Lα source.

The UV-Vis analysis indicates that the GaN nanosheets have a bandgap energy of 3.6 eV as shown in **Figure S1**(a). The bandgap of GaN nanosheets is higher than the bulk GaN.[4] The

photoluminescence and cathodoluminescence spectra reveals the presence of the defect states in the 2D GaN nanosheets as discussed in supporting information (**Figure S1**(b) and (c)).

Chemical state analysis was performed using X-ray photoelectron spectroscopy (XPS) measurements using Ag Lα source where Ga 2p and N 1s core level (CL) spectra are shown in **Figure 1**(h) and (i). The Ga 2p CL spectrum reveals a spin-orbit splitting of 26.9 eV. The peaks positioned at 1118.7 and 1145.6 eV are associated with the Ga $2p_{3/2}$ and Ga $2p_{1/2}$, respectively, which corresponds to GaN. Further, the N 1s CL spectrum has a peak at 397.9 eV, which confirms the chemical interaction of Ga with N in GaN. These peak positions and spin-orbit splitting consistent with the previous literature confirms the synthesis of GaN.[25, 32-33] O 1s CL spectra was also recorded to verify the presence of oxygen with Ga as shown in **Figure S2**. It is observed that there is no chemical interaction between Ga and oxygen suggesting the synthesis of GaN with absence of any gallium oxy-nitride compound.

Electrical and photodetection characteristics were investigated by fabricating two-terminal in-plane devices on the synthesized GaN nanosheets. A schematic of the fabricated device is given in **Figure 2**(a). Large area GaN nanosheets were mesa-etched in rectangular geometry to precisely define the active area of the photodetection device. Firstly, the rectangular patterned resist mask (AZ5241E) was developed using maskless photolithography process. Secondly, inductively coupled plasma-reactive ion etching (ICP-RIE) process with chlorine chemistry was utilised for patterning (see experimental section for detailed fabrication process). The AFM micrographs and the height profiles of the rectangular nanosheets are shown in **Figure S3** (a)–(c). Further, photodetection devices were fabricated using Au/Cr (100/10 nm thick) metal electrodes photo-lithographically patterned on the GaN nanosheets (**Figure 2**(b)) (see experimental section for details). The patterned rectangular GaN nanosheets allow a precise measurement of the active device area which is 2 μm×8 μm. The electrical properties of the fabricated photodetectors were investigated using *I–V* characteristics as shown in **Figure 2**(c). The fabricated device generates larger current once the light source illuminates the device. The difference between the current under illumination and dark condition is termed as photocurrent (ΔI_{DS}). The *I–V* characteristics under dark conditions also suggest a Schottky nature of the metal semiconductor junction of the fabricated device. The photoconductive mode of operation is a dominant mechanism for the

fabricated photodetector which has been discussed in details in later part. An energy band diagram for the fabricated photodetector with and without illumination conditions at zero bias is discussed in Supporting Information (**SI-4**). A plot of current density with varying bias is also shown in the **Figure S4**. The current noise measurements were performed to estimate the noise current density (*NCD*) of the fabricated photodetector (**Figure S4).** This was found to be 4.18×10^{-10} $AHz^{-1/2}$ at 1 Hz.

The fabricated photodetectors were tested for long-term stability by monitoring the photoresponse for 1000 cycles under illumination from an LED source with a wavelength of 365 nm as shown in **Figure 2**(d). It was observed that the photoresponse is reproducible over the course of 1000 cycles. The stable photoresponse over a long period of time makes the device viable for practical applications. The devices were further tested at a varying power density (P_D) from 78 μW/cm^2 to 12 mW/cm^2 under illuminations with a wavelength of 365 nm and bias of 5 V. The supporting information displays transient photoresponse plot of the fabricated device under varying power density of 365 nm (**Figure S5**). The transient photoresponse at 78 μWcm^{-2} is shown in the **Figure S5**(a) where the photodetector exhibits a photocurrent of 0.34 μA, which is stable for repetitive cycles. Transient photoresponse of the fabricated devices under varying P_D from 78 μWcm^{-2} to 12 mW/cm^2 whilst keeping the bias fixed at 5 V are displayed in **Figure S5**(b). A line plot for the photocurrent versus power density is shown in **Figure S5**(c) where the photocurrent increases from 0.34 μA to 0.60 μA whilst varying P_D from 78 μWcm^{-2} to 12 mW cm^{-2}, respectively. The rate of increment in the photocurrent is lower until 1 mW/cm^2 which increases beyond 1mW/cm^2 power density. This is ascribed to an increasing number of incident photons at a higher P_D.

The performance parameters were investigated for benchmarking the fabricated photodetector. Responsivity (*R*) is the measure of the photocurrent generated per input optical power defined by Equation (1).[34]

$$R = \frac{\Delta I_{DS}}{P_D \times A}$$

(1) Here, *A* is the active area of the fabricated device, which is calculated to be 16 μm^2. External quantum efficiency (EQE), which is the photon conversion efficiency, is expressed by Equation (2).[34]

$$EQE = \frac{h \times c \times R}{e \times \lambda}$$

(2) Here, h is the Plank constant, c is the speed of the light, e is the charge of an electron, *and* λ is the incident wavelength. Noise equivalent power, *NEP*, is the lowest incident power that can be detected at a 1 Hz output bandwidth. NEP can be defined by Equation (3).[27]

$$NEP = \frac{i_n}{R} = \frac{(A \times \Delta f)^{1/2}}{D^*} \quad (3)$$

Here, i_n is the noise current, Δf is the bandwidth, and D^* is the specific detectivity is the figure of merit used to characterize the performance of a detector. Specific detectivity (D^*), can be calculated by rearranging Equation (3)

$$D^* = \frac{(A \times \Delta f)^{1/2}}{i_n} \times R \quad (4)$$

The performance of the photodetection devices was analysed by calculating *R* and *EQE* from Equation (1) and (2), respectively. The *R* values increase from 3.15×10^2 A/W to 2.72×10^4 A/W with a decrease in the P_D from 12 mW/cm^2 to 78 μW/cm^2, respectively as shown in **Figure 2**(e).

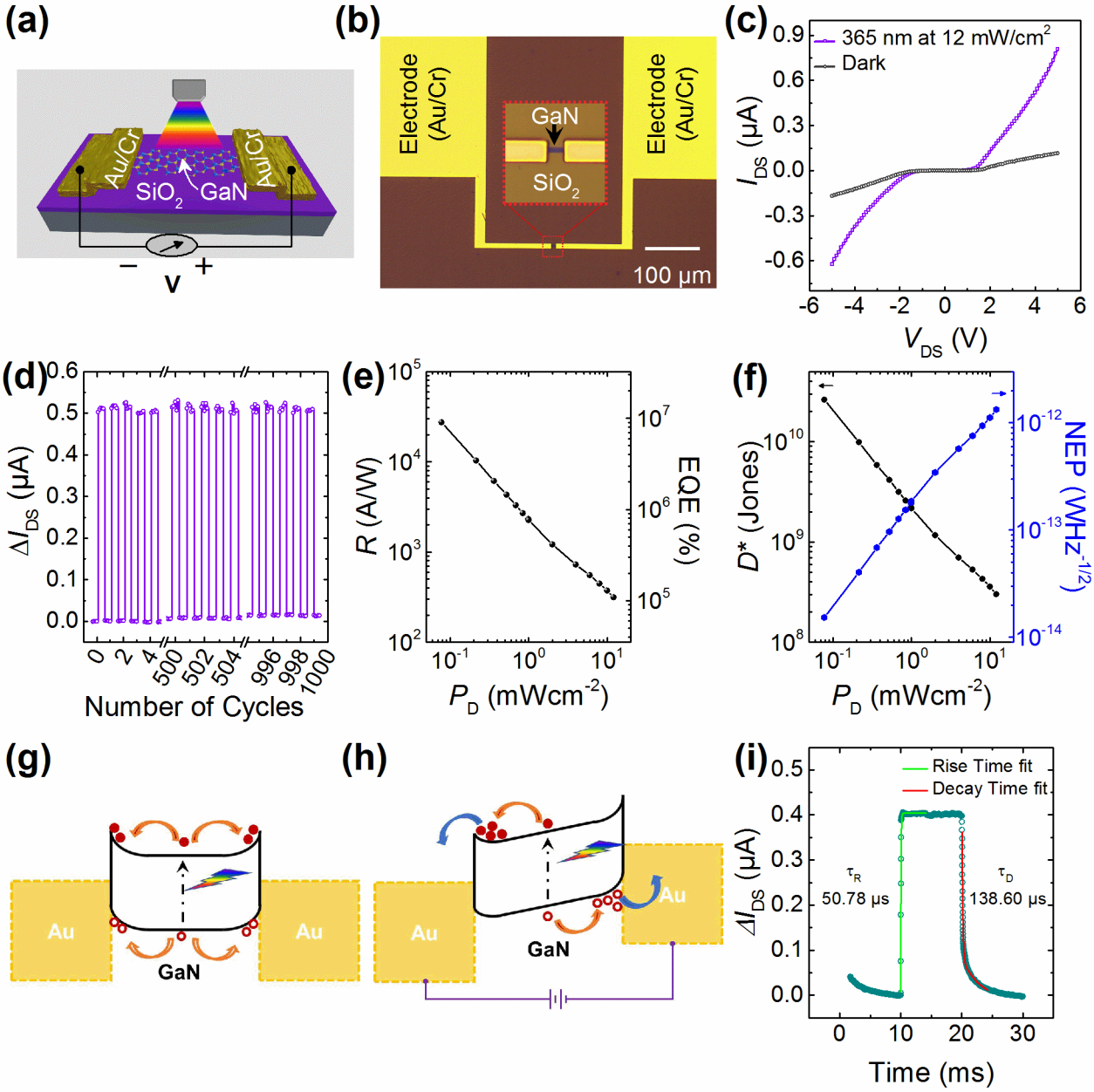

Figure 2. (a) A schematic representation of the fabricated photodetector using GaN nanosheets. (b) An optical image of the fabricated photodetection device on 2D GaN. (c) *I–V* characteristics of the fabricated photodetector under dark and illumination conditions. (d) Transient photoresponse measurements of the 2D GaN photodetection device revealing the stable operation for 1000 repetitive cycles under illuminated at 365 nm with a power density of 12 $mWcm^{-2}$ and 5 V bias. (e) Responsivity & external quantum efficiency and (f) detectivity & noise equivalent power as functions of power density under excitation wavelength, of 365 nm and bias of 5 V. Energy band diagram

suggesting charge transport mechanism under (g) no bias and (h) biased conduction, respectively. (i) Rise and decay time analysis of the 2D GaN device by estimating rise and decay time constant with exponential fitting.

The increment in R with a decrease in P_D is associated to the non-linear behaviour of photocurrent with the P_D. The photogenerated charge carrier concentration reduces at lower P_D but the lifetime of the charge carriers can be increased. This results in the overall increment of R whilst reducing the P_D. The photo to dark current ratio is calculated to be 46.23. This phenomenon illustrates that the fabricated photodetectors are highly sensitive and able to detect low P_D signals. The *EQE* values of the fabricated photodetector are plotted with respect to the P_D in **Figure 2**(e). The *EQE* is proportional to the *R* for a specific wavelength as defined in Equation (2) and follows identical trend to the *R*. The *EQE* increases from 1.07×10^5% to 9.26×10^6% with a decrease in P_D from 12 mWcm^{-2} to 78 μWcm^{-2}, respectively. **Figure 2**(f) plots *D** and *NEP* as a function of P_D. Here, detectivity increases from 3.01×10^8 Jones to 2.61×10^{10} Jones with decreasing the P_D from 12 mWcm^{-2} to 78 μWcm^{-2}, respectively. On the other hand, *NEP* decreases from 1.33×10^{-12} WHz$^{-1/2}$ to 1.53×10^{-14} WHz$^{-1/2}$ with decreasing P_D from 12 mWcm^{-2} to 78 μWcm^{-2}, respectively. The figures of merit suggest that the fabricated photodetector is promising for detecting low power signals efficiently. The atomically thin GaN nanosheets offer higher quantum efficiency owing to quantum confinement with enhanced excitonic effects[24] Further, the large surface to volume ratio of low dimensional GaN nanosheets in comparison to their bulk counterpart potentially offers a longer carrier lifetime and lower recombination probability leading to high responsivity.[35] In addition, the Schottky contacts, as illustrated previously, aid the performance owing to efficient charge separation of photogenerated electron-hole pairs.[36]

The charge transport behaviour of the fabricated GaN photodetector is understood with the help of energy band diagram under no bias and bias condition as depicted in **Figure 2**(g) and (h), respectively. The fabricated photodetector is a metal–semiconductor–metal photodetector geometry with back to back metal–semiconductor electrode junctions. The Au/Cr-GaN interface has a Schottky nature as discussed in previous section. An electron–hole (*e*–*h*) pair is generated by illumination of a photon with sufficient energy for excitation. Under the no-bias condition, the *e*–*h* pairs diffuse toward the junctions in a symmetric manner, therefore

produce no net corrent(**Figure 2**(g)). However, under the bias condition, one of the metal–semiconductor junctions becomes forward biased and another becomes reverse biased as shown in **Figure 2**(h). The potential barrier of the forward–biased metal–semiconductor junction reduces after applied bias. Applied bias results in a potential gradient inside the semiconductors which enables electrons to drift toward one junction and holes toward another junction. These electrons and holes can be collected through the metal electrodes to produce the photocurrent.

The response speed of a photodetector is also an important parameter for signal detection. The fast speed is very crucial in image sensing applications, whereas a slower response is useful for artificial synapse applications.[37-38] The response time can be calculated in terms of the Rise time (T_R) and Decay time (T_D) which is the time required by a photocurrent to reach from 10% to 90% values and vice versa. **Figure 2**(i) exhibits the exponential fit to the photoresponse data recorded at 5 V bias and illumination of 365 nm at 2 mW/cm^2 optical power to analyse the response time of the fabricated devices.[27, 39] The exponential fit provides the values of rise and decay time constants (τ_R and τ_D). The τ_R is the time taken by the photocurrent of a device to achieve 63% of the steady-state value from the initial value. On the other hand, τ_D is the time taken by the photocurrent to reach from the steady-state value to its 63% (37% of the initial photocurrent value). The estimated values of the τ_R and τ_D are 58.78 µs and 138.60 µs, respectively. Further, the T_R and T_D can be calculated by multiplying the τ_R and τ_D with a factor of 2.197, respectively. Subsequently, the T_R and T_D is estimated to be 129.13 µs and 304.50 µs, respectively. The fabricated photodetector displays a fast response speed compared to previously reported devices based on 1D, 2D and 3D semiconductors, as mentioned in **Table** S2. The relatively short response time would be appropriate for the high speed image sensing applications. As mentioned, the T_D is slightly longer in comparison to T_R which is associated to the presence of the defect states. These defect states function as a trapping centre for the photo-generated charge carriers. It ultimately slows down the recombination rate, which leads to a slightly longer decay time and the two aspects could be looked at as a trade-off between speed and responsivity.[4] Further, the response time at microseconds scale omits the possibility of the thermal excitation induced current due to the UV irradiations being the dominant mechanism.

The fabricated photodetectors were further tested under variable bias conditions. The illuminated P_D was fixed at 12 mW/cm^2 with a wavelength of 365 nm and bias was varied from 1 V to 5 V with a step of 1 V. The photoresponse increases with increasing bias, as shown in Supporting Information (**Figure S6**(a)). The *R* and *EQE* were calculated by using Equations (1) and (2), respectively. The *R* and *EQE* increases from 1.48 A/W to 3.15×10^2 A/W and 5.03×10^2% to 1.07×10^5% with an increasein bias from 1 V to 5 V, respectively as illustrated in **Figure S6**(b). The enhancement in the performance parameters with increasing bias conditions can be associated with the enhanced electric field between the metal electrodes. This improved electric field helps in collecting photo-generated charge carriers from the deeper region through the transport channel. The D^* was also calculated for variable bias conditions as discussed in Supporting Information (**Figure S6**(c)). The D^* increases from 1.42×10^6 Jones to 3.01×10^8 Jones and *NEP* decreases from 2.82×10^{10} WHz$^{-1/2}$ to 1.33×10^{-12} AHz$^{-1/2}$ with an increase in the bias from 1 V to 5 V, respectively. It suggests the ability of the photodetector to detect signals at low bias conditions despite the use of atomically thin GaN.

It is crucial to verify the spectral response range to ascertain the practical applicability of the fabricated devices.[40]

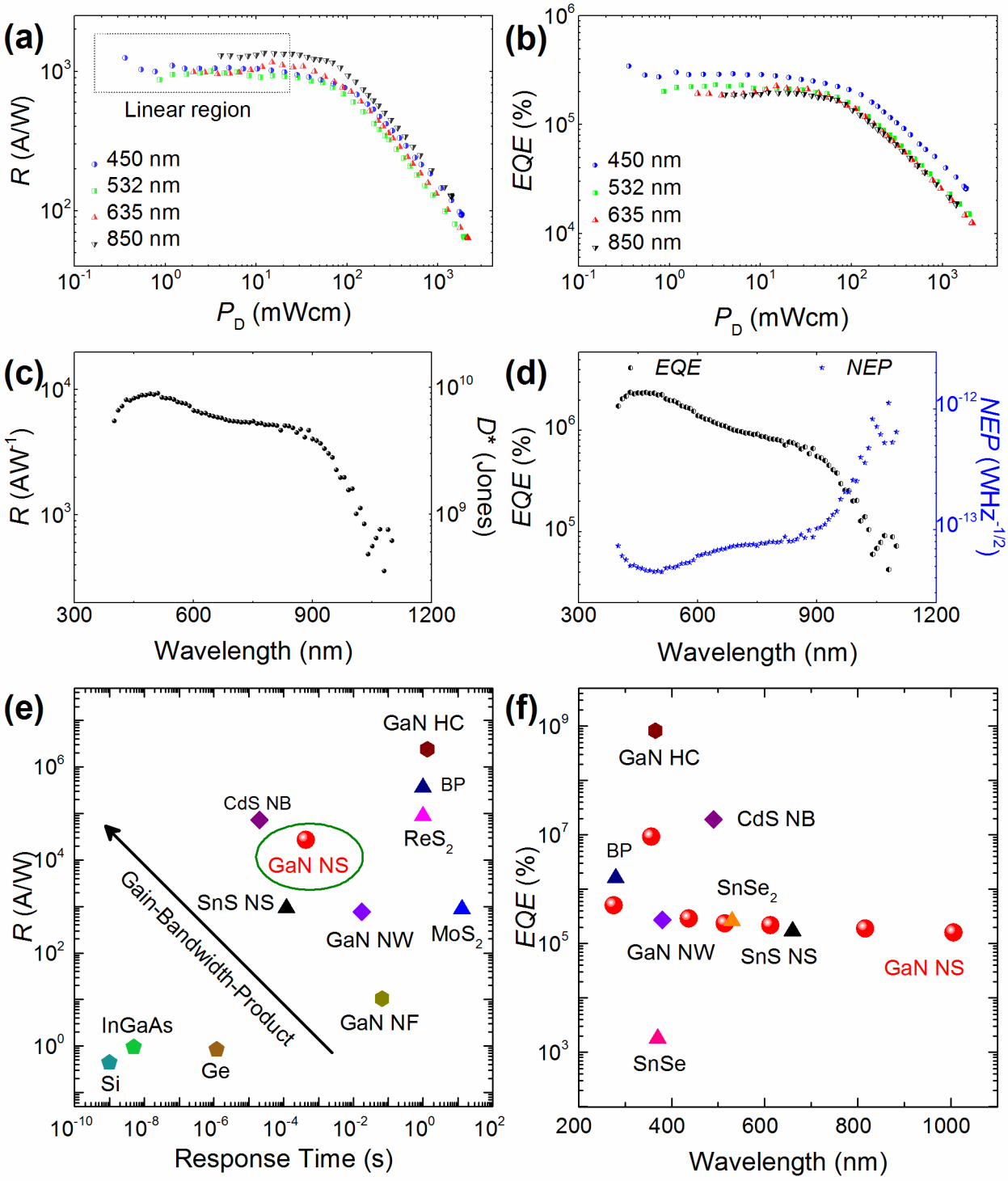

Figure 3. (a) Responsivity and (b) external quantum efficiency plot versus power density under various illumination laser sources. for 2D GaN device. (c) Responsivity & specific detectivity and (d) external quantum efficiency & noise equivalent power plots with varying illumination wavelengths from 400 nm to 1100 nm. (e) A plot showing the responsivity w.r.t. response time where the top left

region corresponds to the high gain-bandwidth product. (f) A plots comparing the external quantum efficiency across the broadband spectrum for various photodetectors. Red spheres, triangles, diamonds, hexagons, and pentagons represent the present work, 2D, 1D, 3D, and commercial photodetectors, respectively. HC – honeycomb; NB – nanobelts; NF – nanoflowers; NS – nanosheets; NW – nanowires.

The fabricated photodetectors were tested from UV (280 nm) to NIR (1080 nm) whilst keeping the bias fixed at 5 V. The ΔI_{DS} versus P_D is plotted illuminated under 450, 532, 635, and 850 nm laser sources as shown in **Figure S7**(a). The plot can be divided into two regions, linear and sub-linear region, corresponding to low and high power density regions, respectively. Further, measurements are performed under the linear regions for better comparison of the responsivity as a function of wavelength. The R versus P_D plot is displayed in **Figure 3**(a) for illumination wavelengths of 450, 532, 635, and 850 nm. The R is nearly constant at lower P_D and decreases while further increasing the P_D. The R values of the fabricated photodetector are recorded as 1.05×10^3, 9.74×10^2, 9.93×10^3, and 1.3×10^3 A/W in the linear region for illumination wavelengths of 450, 532, 635, and 850 nm, respectively. Further, *EQE* are calculated as 2.91×10^5, 2.35×10^5, 2.16×10^5, 1.90×10^5 % for illumination wavelengths of 450, 532, 635, and 850 nm, respectively (Figure 3(b)). The spectral behaviour was further investigated using a broadband laser driven white light source coupled to a monochromator chopped at 70 Hz. The R and D^* are calculated as per the Equation (1) and (4), respectively and plotted as **Figure 3**(c). The photodetector exhibits high R and D^* values of the order of 10^3-10^4 A/W and 10^9-10^{10} Jones, respectively in a broad range from 400 nm to 900 nm. The spectral response displays two peaks at wavelengths of ~490 and 870 nm. The R and D^* values drop for wavelengths longer than 900 nm. It is noted that the spectral response trend is different than discussed in Figure 3(a). The variation in the responsivity is associated to the varying power density values of broadband white light source as shown in Supporting Information (**Figure** S7(b)). Further, *EQE* and *NEP* values are also calculated with the peak *EQE* value being 2.39×10^6 % and the lowest NEP value being 4.47×10^{-14} $WHz^{-1/2}$ as displayed in **Figure 3**(d). It is observed that the *EQE* values for visible and NIR region are lower in comparison to the UV region. This could be associated to the indirect bandgap

nature of the N defect assisted energy levels which offers lower jump rate in visible and NIR region whereas direct bandgap associated energy levels at UV spectrum offer high jump rate.

Our GaN nanosheet based photodetectors display efficient photodetection over a broad spectral range, which is in contrast to conventional GaN photodetectors that only operate in the UV regime.[41-43] The broadband spectral response can be associated with the presence of intermediate energy states inside the forbidden energy gap of the GaN nanosheets. These states are previously observed through photoluminescence and cathodoluminescence spectroscopy measurements. We are able to set a trade–off by incorporating N defects where the spectral response is stretched from UV to NIR spectrum while keeping the response speed of the order of microseconds, which can be deployed for many industrial applications including imaging, communication, and integrated optoelectronic circuits.

DFT calculations were performed to provide further insights into the mechanism of broadband photodetection operation of the GaN nanosheets. A defect-free GaN slab was chosen for the study where the top and side view of the GaN (110) is shown in **Figure 4**(a) and (b), respectively. The thickness of the slab was approximately 1.3 nm which approximately matches that of the LME-synthesised GaN nanosheets as shown in **Figure 1**(d). The top view shows rows of Ga atoms approximately 0.26 nm apart, which is in excellent agreement with the TEM image as shown in **Figure 1**(f). **Figure 4**(c) shows the band structure plot of defect-free GaN slab that depicts a direct (Γ-Γ) bandgap of 3.68 eV, which is close to the experimental observations of the bandgap from the Tauc plot as shown in **Figure S1**. In addition, the Tauc plot shows an absorbance tail at photon energies lower than 3.6 eV, which suggests the presence of a low concentration of defects whose HOMO-LUMO gaps are lower than 3.6 eV. Further, the PL, Cathodoluminescence and spectral response experiments suggest the presence of other defect states in the 2D GaN sheet (see **Figures S1**(b), (c) **and Figure 3**, respectively).

A systematic search for such defects gave three possible defect configurations which may have been observed in the photoluminescence and transient photoresponse experiments. In searching for these defects, we were motivated by the following considerations, (i) the tail of the Tauc plot (**Figure S1**) suggested a low concentration of defects in the GaN 2D layer; (ii) ammonia vapour (NH_3) was present during the transformation of 2D Ga_2O_3 to 2D GaN; (iii)

XPS measurements reveal the absence of Ga-O interaction in the O1s CL level spectra (**Figure S2**) (iv) If the defects in the 2D layer were nitrogen point vacancy defects near the surface, the resulting bonding electrons of the first nearest neighbour Ga atoms could be passivated by a nearby NH_3 molecule or an NH_3 molecular fragment. Using the above ideas as a guide, we found three defect states which all corresponded to an N surface point vacancy defect interacting with a NH_2 molecular species as shown in **Figure 4**(d)-(f). In these Figures, the position of the N atom in a defect-free 2D layer is also indicated (labelled as Vac in the figure). Although Figures 4(d) and (f) look the same visually, there are differences in the relative distances between the atoms (not obvious from the visual representation) that account for the differences in the band structure. **Figure 4** (g)-(i) give the electronic Band Structure (eBS) plots of each of the defect configurations. In these plots, the Valance Band Maximum (VBM) and Conduction Band Minimum (CBM) are shown as dashed lines. Each plot shows that the defect state gives rise to an indirect bandgap and results in semiconductor p-type behaviour as the Fermi level (set at 0 eV) in each case is close to the VBM. As stated earlier, the existence of these defects is feasible as it is conceivable that surface point vacancies may be formed during the fabrication of the 2D nanosheets and ammonia vapour (NH_3) was present during the formation of the 2D GaN layer.

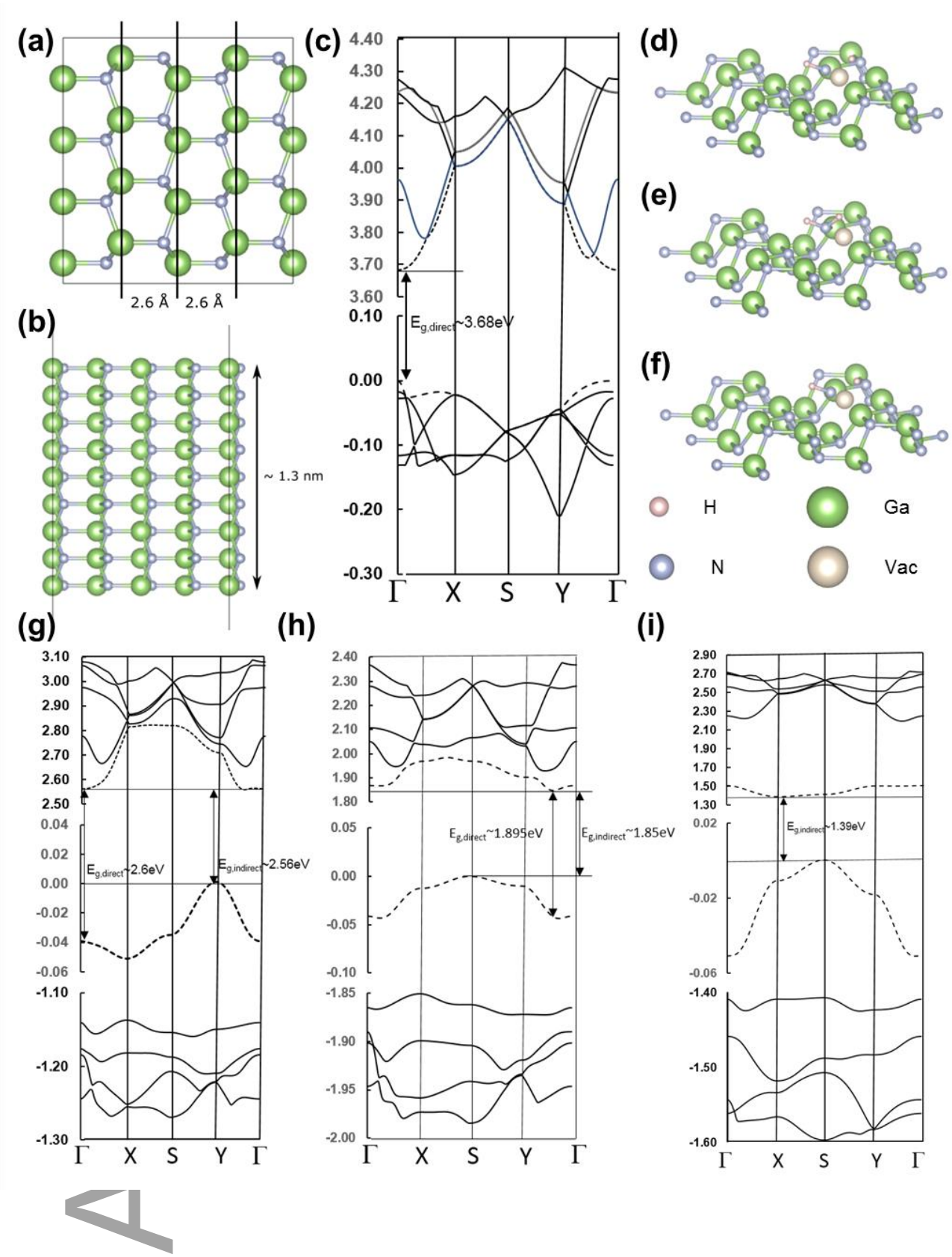

Figure 4. DFT Analysis of 2D GaN (110) (a) Top view and (b) side view. (c) Electronic Band structure plot of the 1.3nm defect-free GaN(110) slab showing a direct bandgap of 3.68 eV. In the BS plot the Valance Band Maximum (VBM) and Conduction Band Minimum (CBM) are shown as dashed lines. (d)-(f) different defect configurations correspond to a surface N point vacancy interacting with an NH_2 molecule. In (g)-(i) Band structure plots are shown for the 3 defect configurations corresponding to (d)-(f), respectively. Each of the defect states result in indirect bandgap values of (d) 2.56 eV, (e) 1.85 eV, and (f) 1.39 eV.

If we assume that the probability of formation of these defect configurations (relative to the N-point vacancy slab and nearby NH_3) is proportional to $exp\left(\frac{\Delta E}{k_B T}\right)$ where ΔE is the defect formation energy of the defect state, k_B is Boltzmann's constant, and T is the temperature.[44-45] We can estimate the relative probabilities for the formation of these defects at 300K as shown in **Table S1**. The fact that these formation probabilities are small is again consistent with the Tauc plot (**Figure S1**(a)). These 3 defect states corresponds to the energy gap of 1.39, 1.85, and 2.56 eV, corresponding to 892, 670, and 484 nm wavelengths, respectively. **Figure 3**(b) displays spectral response in a broad wavelength range thant spans 400 to 900 nm, and droping for longer wavelengths. Moreover, two peaks are observed at wavelengths of ~490 and 870 nm, which is very close to the defect states (2.56 eV and 1.39 eV) observed in DFT. The defect states observed at 490 and 670 nm via DFT calculations are in close correlation to the defect states observed in cathodoluminescence (2.63 and 1.88 eV) and PL (1.89 eV) spectroscopy.

We conjecture that an explanation for this is as follows; (i) All 3 defect configurations result in indirect bandgaps (**Figure 4**(g)-(i)); (ii) Radiative transitions in indirect bandgap materials is a second order process which requires the absorption/emission of a photon and a phonon (from the lattice) in order to satisfy conservation of momentum and energy, while in direct bandgap materials only the absorption/emission of a photon is required (a first order process as no phonons are involved); (iii) it follows from (ii) that the transition rate for absorption/emission of a photon (leading to the promotion of an electron from the valance to the conduction band) in a direct bandgap material (1^{st} order process) is much higher than that for indirect bandgap materials (which occur via 2^{nd} order processes); (iv) for the defect states corresponding to 1.39, 1.89, and 2.56 eV band structure plots show that the energy difference

between the indirect and direct gaps is ~40 meV, (v) 40meV is approximately the average thermal kinetic energy of an electron at 300 K, thus the kinetic energy of an electron in the VBM is enough to make a vertical (direct) transition to the CBM for all the three defect states, leading to a higher photocurrent for these defect states. These insights into the operating mechanism also highlight the opportunities to tune the properties of the GaN by modulating the synthesis conditions particularly the N_2 concentration.

If we benchmark the performance of our GaN based photodetector to other reported and commercial devices, it reveals that the high figure of merits are achieved using the ultrathin photoactive GaN layer. A comparison chart for the performance metrics of the fabricated photodetector with the previous reports is shown in **Figure 3**(d)-(e). A table for the comparison of the state-of-the-art performance parameters is shown in the supporting information (**Table S2**). The performance of the novel photodetectors is reasonable good compared to previous conventional GaN based photodetectors.[4, 46-48] The present devices display responsivity 10^3-10^4 times higher than the GaN photodetectors fabricated with epitaxial planar thin films.[46] Epitaxial thin films consist dislocations, which leads to the excess leakage current.[48] Recently, the performance of the GaN photodetectors was improved by modifying the surface structure and growing thicker films.[4, 47] It is notable that the present ultrathin GaN nanosheets are 4×10^3 times thinner than previous epitaxial GaN films. One of the major challenges is the trade-off between the responsivity and the speed of the photodetector, where the present devices exhibit superior performance, as shown in **Figure 3**(d). Further, other 2D photodetectors demonstrates the responsivity and EQE in the range of 10^0–10^5 A/W and 10^1–10^7%, respectively, as shown in **Figure 3**(d) and (e) (also mentioned in Table S2). However, these material platforms are facing several challenges. For instance, cadmium sulphide (CdS) nanobelts are hundreds of micrometres in length and 200 nm thick which is much higher than the present study.[49] Moreover, Cadmium being a heavy metal, is very hazardous and toxic. Black phosphorous is facing a key issue of the degradation under the ambient environment whereas MoS_2 based photodetectors are struggling with a slower response time due to low electron mobility.[50-51] The commercial photodetectors have also been compromising on various aspects including thick material requirements, inability to detect a broader spectrum at low intensities, higher defect density, and incompatibility with

flexible platforms.[52-53] Therefore, the present study offers a commercially viable and stable platform to serve the high demand for the broadband photodetection applications.

Conclusions

In summary, millimetre-scale ultrathin (~1.4 nm) 2D GaN nanosheets were synthesised *via* a simple two-step LME method and broadband photodetection properties were investigated via 2-terminal photodetection devices. DFT calculations suggest presence of N-point vacancy defects in the GaN nanosheets, that enable a broadband photodetection of GaN from UV (280 nm) to NIR (1050) spectrum region. The fabricated photodetectors displayed a peak responsivity of 2.72×10^4 A/W illuminated at a wavelength of 365 nm along with a fast responsive speed of the order of 10^2 µs. The ultrathin GaN based photodetector demonstrated excellent figures-of-merit in comparison to the commercial photodetectors with Si, Ge, and InGaAs material platforms. The responsivity is up to 10^4 orders higher whilst comparable specific detectivity values of the ultrathin photodetectors.. The present study opens a new vista of the GaN platform, expanding its applications towards the miniaturized device technology for imaging systems, spectroscopy, communication, and integrated circuits.

Materials and Methods

Synthesis of 2D GaN Nanosheets

(a) Squeeze-printing process of the 2D Ga_2O_3 sheets

Homogeneous ultra-thin gallium oxide sheets were exfoliated from liquid metal droplets on suitable substrate using the liquid metal based Van der Waal printing technique. The van der Waals attachment between gallium oxides and the substrate delaminates the oxide skin formed on the surface of the droplet. Metal inclusions on the exfoliated sheets could be removed using the previously reported solvent assisted cleaning method.[25] High-quality Ga_2O_3 sheets with large lateral dimensions of more than several centimetres could be efficiently exfoliated on both substrates with this squeeze printing method.

(b) Transformation of 2D Ga_2O_3 to 2D GaN sheets via ammonolysis process

An ammonolysis reaction method was utilized for transforming the gallium oxide sheets into gallium nitride sheets. This was performed in a quartz tube placed in a horizontal tubular furnace where the 2D Ga_2O_3 samples reacted with ammonia vapor to grow the 2D GaN films. Urea pellets were used as a source material for the production of NH_3 gas and N_2 gas with a flow rate of 50 sccm was used as the carrier gas. The entire reaction was conducted for 75 minutes after the temperature of the system had reached 900 °C. Next the synthesized GaN samples were then cooled to room temperature and stored in nitrogen purged glovebox or vacuum desiccators.

Material Characterizations

The low and high resolution TEM measurements were performed using a JEOL 1010 and a JEOL 2100F with acceleration voltages of 100 and 200 kV, respectively. Gatan microscopy suite 1.8.4. Software Package was used for TEM/HRTEM analysis. High temperature resistant Si_3N_4 (Ted Pella, 21587-10) TEM membranes were used to develop the TEM samples that were prepared by directly printing the gallium oxide sheet onto TEM membrane and subsequent ammonolysis. Surface chemistry was investigated by XPS measurements using a Kratos AXIS Supra XPS spectrometer equipped with a monochromatic Ag Lα source (hν=2984.3 eV) with a pass energy of 80 eV. A charge neutraliser was used to eliminate the surface charging effect. AFM image was obtained using Bruker Dimension Icon using "ScanAsyst-air" AFM tips. UV-Vis measurements of the samples deposited on quartz were conducted on an Agilent Cary 60 spectrophotometer and on an Agilent Cary 7000 spectrophotometer equipped with an integrating sphere to account for scattering contribution. Room temperature PL measurements were performed on a custom-built confocal PL setup under 532 nm continuous laser excitation. Cathodoluminescence spectra were collected using a Delmic SPARC system with a 13 mm parabolic mirror. Data was collected with a 2 keV beam energy and 0.28-1.0 beam current. Cathodoluminescence emission was sent to a UV-visible spectrometer equipped with a 300 lines/mm grating. Delmic Odemis software was used for data collection.

DFT Calculations

A GaN wurtzite bulk supercell was constructed using crystallography information provided by the open crystallography database (CIF file 9008868) [1]. Hybrid Density Functional Theory calculations were performed using Gaussian basis set abinitio package CRYSTAL14 [2,3]. The PBEsol0 hybrid exchange-correlation functional, (which uses the PBE functional revised for solids (PBEsol) [4] with 25% Hartree-Fock exact exchange) was used to calculate the slab energies and Electronic Density of States. For all atoms a Triple Zeta Valance basis set (TZV), with polarization functions, was used to model the electrons [5]. Band structure and energy calculations were conducted using a 9x9x1 Monkhorst-Pack k-point mesh. Van der Waal dispersion corrections to the energy were performed using the method proposed by Grimme [6]. For the slab calculations, a periodic slab of GaN of thickness ~1.3nm with a non-polar (110) surface was cut from the wurtzite bulk phase. The slab was rectangular in shape corresponding to the plane group symmetry p1g1 and therefore for the band structure plots we used the following high symmetry points corresponding to the in-plane paths of a simple orthorhombic BZ, Γ(000), X(1/2,0,0), S(1/2,1/2,0), Y(0,1/2,0).

Device Fabrication and Testing

The synthesised GaN nanosheets were patterned using inductive coupled plasma (ICP) - reactive ion etching (RIE) process. The as synthesised GaN nanosheets were first chemically cleaned by sequentially ultrasonicating in Acetone, Iso-propanol, and DI water for 10 minutes each followed by blown dry with N_2. AZ5214E photoresist was spin coated on the samples and placed under the MLA 150 system and etch patterns were exposed and developed onto the samples. The photoresist patterned (used as a hard mask) 2D-GaN samples were placed in the DRIE Multi Oxford plasmaLab system 100 (ICP-RIE system). BCl_3/Cl_2/Ar gas ratio was set at 8/30/4 at an ICP power of 500 W. RF power was set to 40 W with a chamber pressure of 2 mTorr. The sample stage was kept at 10 °C and etching was performed for 90 s. The etched pattern was characterised by AFM measurements as discussed in supporting information (**Figure S3**). The patterns having a width and length of 2 µm and 12 µm, were etched up to a depth of 21 nm to assure that only the defined area is contributing to the photoresponse measurements. Further, two-terminal metal electrodes were deposited on these

patterned GaN samples. Firsly, metal electrode patterns were aligned and developed using AZ5214E photoresist on the rectangular GaN nanosheets and then Au/Cr (having a thickness of 100/10 nm) metal electrodes were deposited using e-beam evaporation process. An optical image of the fabricated devices is shown in **Figure 2**(b). Photoresponse measurements at 280, 365, and 365 nm were performed using monochromatic LED sources (Thorlabs, Inc.) and 450, 532, 635, 850 were performed using laser sources. The spectral responsivity was determined using a broadband laser driven white light source coupled to a monochromator. The light was mechanically chopped at 70 Hz and the wavelength was scanned at 10nm steps from 400 to 1100 nm. Photocurrent was measured using the lock in technique at each waveelngth. Agilent 2912A source meter was used for the electrical measurements under both dark and illumination conditions.

Acknowledgements

SKJ would like to acknowledge Joint RMIT-AcSIR PhD scholarship program for financial assistance. This work was performed in part at the Micro Nano Research Facility at RMIT University and the Melbourne Centre for Nanofabrication (MCN) in the Victorian Node of the Australian National Fabrication Facility (ANFF). Facilities and technical support from the RMIT Microscopy and Microanalysis Facility, a linked laboratory of Microscopy Australia, is acknowledged. SW acknowledges project support through the ARC Discovery Projects Scheme (DP220100020). SPR acknowledges the support of the Australian Government through the Australian Research Council (ARC) under the Centre of Excellence scheme (CE170100026). This work was also supported by computational resources provided by the Australian Government through the National Computational Infrastructure National Facility and the Pawsey Supercomputer Centre. N. Syed recognizes the support of the McKenzie Postdoctoral Fellowship from the University of Melbourne. K.B.C. and M.B. acknowledge the support of the Australian Government through the ARC under the Centre of Excellence scheme (CE200100010). Authors would like to acknowledge Mark Lockrey and Mehran Kianinia for assistance with the Cathodoluminescence and PL measurements and Prof Sharath Sriram for the useful discussions.

References

1. Zheng, Z.; Zhang, L.; Song, W.; Feng, S.; Xu, H.; Sun, J.; Yang, S.; Chen, T.; Wei, J.; Chen, K. J., Gallium nitride-based complementary logic integrated circuits. *Nature Electronics* **2021,** *4* (8), 595-603.

2. Amano, H.; Baines, Y.; Beam, E.; Borga, M.; Bouchet, T.; Chalker, P. R.; Charles, M.; Chen, K. J.; Chowdhury, N.; Chu, R.; De Santi, C.; De Souza, M. M.; Decoutere, S.; Di Cioccio, L.; Eckardt, B.; Egawa, T.; Fay, P.; Freedsman, J. J.; Guido, L.; Häberlen, O.; Haynes, G.; Heckel, T.; Hemakumara, D.; Houston, P.; Hu, J.; Hua, M.; Huang, Q.; Huang, A.; Jiang, S.; Kawai, H.; Kinzer, D.; Kuball, M.; Kumar, A.; Lee, K. B.; Li, X.; Marcon, D.; März, M.; McCarthy, R.; Meneghesso, G.; Meneghini, M.; Morvan, E.; Nakajima, A.; Narayanan, E. M. S.; Oliver, S.; Palacios, T.; Piedra, D.; Plissonnier, M.; Reddy, R.; Sun, M.; Thayne, I.; Torres, A.; Trivellin, N.; Unni, V.; Uren, M. J.; Van Hove, M.; Wallis, D. J.; Wang, J.; Xie, J.; Yagi, S.; Yang, S.; Youtsey, C.; Yu, R.; Zanoni, E.; Zeltner, S.; Zhang, Y., The 2018 GaN power electronics roadmap. *J. Phys. D: Appl. Phys.* **2018,** *51* (16), 163001.

3. Chen, Z.; Liu, Z.; Wei, T.; Yang, S.; Dou, Z.; Wang, Y.; Ci, H.; Chang, H.; Qi, Y.; Yan, J.; Wang, J.; Zhang, Y.; Gao, P.; Li, J.; Liu, Z., Improved Epitaxy of AlN Film for Deep-Ultraviolet Light-Emitting Diodes Enabled by Graphene. *Adv. Mater.* **2019,** *31* (23), 1807345.

4. Jain, S. K.; Low, M. X.; Vashishtha, P.; Nirantar, S.; Zhu, L.; Ton-That, C.; Ahmed, T.; Sriram, S.; Walia, S.; Gupta, G.; Bhaskaran, M., Influence of Temperature on Photodetection Properties of Honeycomb-like GaN Nanostructures. *Advanced Materials Interfaces* **2021,** *8* (14), 2100593.

5. Zhu, D.; Wallis, D. J.; Humphreys, C. J., Prospects of III-nitride optoelectronics grown on Si. *Rep. Prog. Phys.* **2013,** *76* (10), 106501.

6. Ponce, F. A.; Bour, D. P., Nitride-based semiconductors for blue and green light-emitting devices. *Nature* **1997,** *386* (6623), 351-359.

7. Westover, T.; Jones, R.; Huang, J. Y.; Wang, G.; Lai, E.; Talin, A. A., Photoluminescence, Thermal Transport, and Breakdown in Joule-Heated GaN Nanowires. *Nano Lett.* **2009,** *9* (1), 257-263.

8. Morkoç, H., General Properties of Nitrides. In *In Handbook of Nitride Semiconductors and Devices*, 2009.

9. Thomas, S., Gallium nitride gets wrapped up. *Nature Electronics* **2020,** *3* (12), 729-729.

10. Zhang, S.; Ma, B.; Zhou, X.; Hua, Q.; Gong, J.; Liu, T.; Cui, X.; Zhu, J.; Guo, W.; Jing, L.; Hu, W.; Wang, Z. L., Strain-controlled power devices as inspired by human reflex. *Nature Communications* **2020,** *11* (1), 326.

11. Aggarwal, N.; Krishna, S. T. C.; Goswami, L.; Mishra, M.; Gupta, G.; Maurya, K. K.; Singh, S.; Dilawar, N.; Kaur, M., Extenuation of Stress and Defects in GaN Films Grown on a Metal–Organic Chemical

Vapor Deposition-GaN/c-Sapphire Substrate by Plasma-Assisted Molecular Beam Epitaxy. *Cryst. Growth Des.* **2015,** *15* (5), 2144-2150.

12. Rabiee Golgir, H.; Li, D. W.; Keramatnejad, K.; Zou, Q. M.; Xiao, J.; Wang, F.; Jiang, L.; Silvain, J.-F.; Lu, Y. F., Fast Growth of GaN Epilayers via Laser-Assisted Metal–Organic Chemical Vapor Deposition for Ultraviolet Photodetector Applications. *ACS Appl. Mater. Interfaces* **2017,** *9* (25), 21539-21547.

13. Zhao, J.-W.; Zhang, Y.-F.; Li, Y.-H.; Su, C.-h.; Song, X.-M.; Yan, H.; Wang, R.-Z., A low cost, green method to synthesize GaN nanowires. *Sci. Rep.* **2015,** *5* (1), 17692.

14. Deng, D.; Novoselov, K. S.; Fu, Q.; Zheng, N.; Tian, Z.; Bao, X., Catalysis with two-dimensional materials and their heterostructures. *Nat. Nanotechnol.* **2016,** *11* (3), 218-230.

15. Choi, W.; Choudhary, N.; Han, G. H.; Park, J.; Akinwande, D.; Lee, Y. H., Recent development of two-dimensional transition metal dichalcogenides and their applications. *Mater. Today* **2017,** *20* (3), 116-130.

16. Khan, K.; Tareen, A. K.; Aslam, M.; Wang, R.; Zhang, Y.; Mahmood, A.; Ouyang, Z.; Zhang, H.; Guo, Z., Recent developments in emerging two-dimensional materials and their applications. *J. Mater. Chem. C* **2020,** *8* (2), 387-440.

17. Wang, W.; Jiang, H.; Li, L.; Li, G., Two-dimensional group-III nitrides and devices: a critical review. *Rep. Prog. Phys.* **2021,** *84* (8), 086501.

18. Wang, Q. H.; Kalantar-Zadeh, K.; Kis, A.; Coleman, J. N.; Strano, M. S., Electronics and optoelectronics of two-dimensional transition metal dichalcogenides. *Nat. Nanotechnol.* **2012,** *7* (11), 699-712.

19. Kang, S.; Lee, D.; Kim, J.; Capasso, A.; Kang, H. S.; Park, J.-W.; Lee, C.-H.; Lee, G.-H., 2D semiconducting materials for electronic and optoelectronic applications: potential and challenge. *2D Materials* **2020,** *7* (2), 022003.

20. Mak, K. F.; Shan, J., Photonics and optoelectronics of 2D semiconductor transition metal dichalcogenides. *Nature Photonics* **2016,** *10* (4), 216-226.

21. Koratkar, N. A., Two-dimensional gallium nitride. *Nature Materials* **2016,** *15* (11), 1153-1154.

22. Sanders, N.; Bayerl, D.; Shi, G.; Mengle, K. A.; Kioupakis, E., Electronic and Optical Properties of Two-Dimensional GaN from First-Principles. *Nano Lett.* **2017,** *17* (12), 7345-7349.

23. Moram, M. A.; Vickers, M. E., X-ray diffraction of III-nitrides. *Rep. Prog. Phys.* **2009,** *72* (3), 036502.

24. Al Balushi, Z. Y.; Wang, K.; Ghosh, R. K.; Vilá, R. A.; Eichfeld, S. M.; Caldwell, J. D.; Qin, X.; Lin, Y.-C.; DeSario, P. A.; Stone, G.; Subramanian, S.; Paul, D. F.; Wallace, R. M.; Datta, S.; Redwing, Joan M.; Robinson, J. A., Two-dimensional gallium nitride realized via graphene encapsulation. *Nature Materials* **2016,** *15* (11), 1166-1171.

25. Syed, N.; Zavabeti, A.; Messalea, K. A.; Della Gaspera, E.; Elbourne, A.; Jannat, A.; Mohiuddin, M.; Zhang, B. Y.; Zheng, G.; Wang, L.; Russo, S. P.; Dorna, E.; McConville, C. F.; Kalantar-Zadeh, K.; Daeneke, T., Wafer-Sized Ultrathin Gallium and Indium Nitride Nanosheets through the Ammonolysis of Liquid Metal Derived Oxides. *J. Am. Chem. Soc.* **2019,** *141* (1), 104-108.

26. Chen, Y.; Liu, K.; Liu, J.; Lv, T.; Wei, B.; Zhang, T.; Zeng, M.; Wang, Z.; Fu, L., Growth of 2D GaN Single Crystals on Liquid Metals. *J. Am. Chem. Soc.* **2018,** *140* (48), 16392-16395.

27. Krishnamurthi, V.; Khan, H.; Ahmed, T.; Zavabeti, A.; Tawfik, S. A.; Jain, S. K.; Spencer, M. J. S.; Balendhran, S.; Crozier, K. B.; Li, Z.; Fu, L.; Mohiuddin, M.; Low, M. X.; Shabbir, B.; Boes, A.; Mitchell, A.; McConville, C. F.; Li, Y.; Kalantar-Zadeh, K.; Mahmood, N.; Walia, S., Liquid-Metal Synthesized Ultrathin SnS Layers for High-Performance Broadband Photodetectors. *Adv. Mater.* **2020,** *32* (45), 2004247.

28. Zavabeti, A.; Ou, J. Z.; Carey, B. J.; Syed, N.; Orrell-Trigg, R.; Mayes, E. L. H.; Xu, C.; Kavehei, O.; O'Mullane, A. P.; Kaner, R. B.; Kalantar-zadeh, K.; Daeneke, T., A liquid metal reaction environment for the room-temperature synthesis of atomically thin metal oxides. *Science* **2017,** *358* (6361), 332-335.

29. Syed, N.; Zavabeti, A.; Ou, J. Z.; Mohiuddin, M.; Pillai, N.; Carey, B. J.; Zhang, B. Y.; Datta, R. S.; Jannat, A.; Haque, F.; Messalea, K. A.; Xu, C.; Russo, S. P.; McConville, C. F.; Daeneke, T.; Kalantar-Zadeh, K., Printing two-dimensional gallium phosphate out of liquid metal. *Nat. Commun.* **2018,** *9* (1), 3618.

30. Ketchum, D. R.; Kolis, J. W., Crystal growth of gallium nitride in supercritical ammonia. *J. Cryst. Growth* **2001,** *222* (3), 431-434.

31. Seo, H. W.; Bae, S. Y.; Park, J.; Yang, H.; Park, K. S.; Kim, S., Strained gallium nitride nanowires. *J. Chem. Phys* **2002,** *116* (21), 9492-9499.

32. Yadav, B. S.; Major, S. S.; Srinivasa, R. S., Growth and structure of sputtered gallium nitride films. *J. Appl. Phys.* **2007,** *102* (7), 073516.

33. Chang, L.-W.; Chang, J.-H.; Yeh, J.-W.; Lin, H.-N.; Shih, H. C., Zigzag GaN/Ga2O3 heterogeneous nanowires: Synthesis, optical and gas sensing properties. *AIP Advances* **2011,** *1* (3), 032114.

34. Kong, W.-Y.; Wu, G.-A.; Wang, K.-Y.; Zhang, T.-F.; Zou, Y.-F.; Wang, D.-D.; Luo, L.-B., Graphene-β-Ga2O3 Heterojunction for Highly Sensitive Deep UV Photodetector Application. *Adv. Mater.* **2016,** *28* (48), 10725-10731.

35. Wang, H.; Zhang, C.; Rana, F., Surface Recombination Limited Lifetimes of Photoexcited Carriers in Few-Layer Transition Metal Dichalcogenide MoS2. *Nano Lett.* **2015,** *15* (12), 8204-8210.

36. Zhou, J.; Gu, Y.; Hu, Y.; Mai, W.; Yeh, P.-H.; Bao, G.; Sood, A. K.; Polla, D. L.; Wang, Z. L., Gigantic enhancement in response and reset time of ZnO UV nanosensor by utilizing Schottky contact and surface functionalization. *Appl. Phys. Lett.* **2009,** *94* (19), 191103.

37. Gong, X.; Tong, M.; Xia, Y.; Cai, W.; Moon, J. S.; Cao, Y.; Yu, G.; Shieh, C.-L.; Nilsson, B.; Heeger, A. J., High-Detectivity Polymer Photodetectors with Spectral Response from 300 nm to 1450 nm. *Science* **2009,** *325* (5948), 1665.

38. Krishnamurthi, V.; Ahmed, T.; Mohiuddin, M.; Zavabeti, A.; Pillai, N.; McConville, C. F.; Mahmood, N.; Walia, S., A Visible-Blind Photodetector and Artificial Optoelectronic Synapse Using Liquid-Metal Exfoliated ZnO Nanosheets. *Adv. Opt. Mater.* **2021,** *n/a* (n/a), 2100449.

39. Gundimeda, A.; Krishna, S.; Aggarwal, N.; Sharma, A.; Sharma, N. D.; Maurya, K. K.; Husale, S.; Gupta, G., Fabrication of non-polar GaN based highly responsive and fast UV photodetector. *Appl. Phys. Lett.* **2017,** *110* (10), 103507.

40. Li, C.; Wang, H.; Wang, F.; Li, T.; Xu, M.; Wang, H.; Wang, Z.; Zhan, X.; Hu, W.; Shen, L., Ultrafast and broadband photodetectors based on a perovskite/organic bulk heterojunction for large-dynamic-range imaging. *Light Sci. Appl.* **2020,** *9* (1), 31.

41. Sun, X.; Li, D.; Li, Z.; Song, H.; Jiang, H.; Chen, Y.; Miao, G.; Zhang, Z., High spectral response of self-driven GaN-based detectors by controlling the contact barrier height. *Sci. Rep.* **2015,** *5* (1), 16819.

42. Goswami, L.; Aggarwal, N.; Vashishtha, P.; Jain, S. K.; Nirantar, S.; Ahmed, J.; Khan, M. A. M.; Pandey, R.; Gupta, G., Fabrication of GaN nano-towers based self-powered UV photodetector. *Sci. Rep.* **2021,** *11* (1), 10859.

43. Chen, X.-X.; Xiao, X.-H.; Shi, Z.-F.; Du, R.; Li, X.-J., Self-powered ultraviolet photodetection realized by GaN/Si nanoheterostructure based on silicon nanoporous pillar array. *J. Alloys Compd.* **2018,** *767*, 368-373.

44. Webber, B. T.; Per, M. C.; Drumm, D. W.; Hollenberg, L. C. L.; Russo, S. P., Ab initio thermodynamics calculation of the relative concentration of NV${}^{\ensuremath{-}}$ and NV^{0} defects in diamond. *Physical Review B* **2012,** *85* (1), 014102.

45. Lu, Y. H.; Hong, Z. X.; Feng, Y. P.; Russo, S. P., Roles of carbon in light emission of ZnO. *Appl. Phys. Lett.* **2010,** *96* (9), 091914.

46. Jain, S. K.; Aggarwal, N.; Krishna, S.; Kumar, R.; Husale, S.; Gupta, V.; Gupta, G., GaN-UV photodetector integrated with asymmetric metal semiconductor metal structure for enhanced responsivity. *J. Mater. Sci.: Mater. Electron.* **2018,** *29* (11), 8958-8963.

47. Aggarwal, N.; Krishna, S.; Sharma, A.; Goswami, L.; Kumar, D.; Husale, S.; Gupta, G., A Highly Responsive Self-Driven UV Photodetector Using GaN Nanoflowers. *Adv. Electron. Mater.* **2017,** *3* (5), 1700036.

48. Aggarwal, N.; Krishna, S.; Goswami, L.; Gupta, G., Inclination of screw dislocations on the performance of homoepitaxial GaN based UV photodetectors. *Materials Science and Engineering: B* **2021,** *263*, 114879.

49. Li, L.; Wu, P.; Fang, X.; Zhai, T.; Dai, L.; Liao, M.; Koide, Y.; Wang, H.; Bando, Y.; Golberg, D., Single-Crystalline CdS Nanobelts for Excellent Field-Emitters and Ultrahigh Quantum-Efficiency Photodetectors. *Adv. Mater.* **2010,** *22* (29), 3161-3165.

50. Ahmed, T.; Balendhran, S.; Karim, M. N.; Mayes, E. L. H.; Field, M. R.; Ramanathan, R.; Singh, M.; Bansal, V.; Sriram, S.; Bhaskaran, M.; Walia, S., Degradation of black phosphorus is contingent on UV–blue light exposure. *npj 2D Materials and Applications* **2017,** *1* (1), 18.

51. Lopez-Sanchez, O.; Lembke, D.; Kayci, M.; Radenovic, A.; Kis, A., Ultrasensitive photodetectors based on monolayer MoS2. *Nat. Nanotechnol.* **2013,** *8* (7), 497-501.

52. Saran, R.; Curry, R. J., Lead sulphide nanocrystal photodetector technologies. *Nature Photonics* **2016,** *10* (2), 81-92.

53. Konstantatos, G.; Sargent, E. H., Solution-Processed Quantum Dot Photodetectors. *Proc. IEEE* **2009,** *97* (10), 1666-1683.

TOC

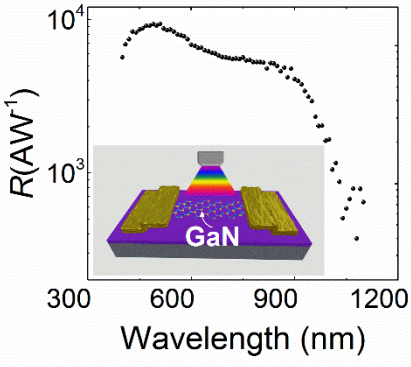

A broadband micro-photodetector is fabricated using atomically thin gallium nitride nanosheets coupled with nitrogen point vacancies covering UV (280 nm) to NIR (1080 nm) spectral width. The fabricated device displays responsivity ~10^4 orders higher than the commercial photodetectors at room temperature, despite being 10^2-10^3 orders thinner that can be deployed in high-performance miniaturised imaging systems, communication and integrated optoelectronics.